Driving Mechanisms of High-Speed Unsteady Spiked Body Flows, Part 1: Pulsation Mode

Daniel Feszty,* Ken J. Badcock,† and Bryan E. Richards‡
University of Glasgow, Glasgow, Scotland G12 8QQ, United Kingdom

The driving mechanism of the unsteady flow mode pulsation arising over axisymmetric spiked bodies has been analyzed by using computational fluid dynamics as a tool. Laminar, axisymmetric flow at Mach 2.21 and Reynolds number (based on the blunt-body diameter) of 0.12×10^6 was simulated by a spatially and temporally second-order-accurate finite volume method. The model geometry was a forward facing cylinder of diameter D equipped with a spike of length $L/D = 1.00$. After reviewing previous pulsation hypotheses, the numerical results were analyzed in detail. A new driving mechanism was proposed, its main features being the creation of a vortical region in the vicinity of the foreshock-aftershock intersection causing mass influx into the dead-air region, the existence of supersonic flow within the dead-air region, the liftoff of the shear layer from the spike tip, and the collision of the recirculated and penetrating flows within the expanded separated region.

Nomenclature

a = nondimensional speed of sound a^*/u_∞^*
D = nondimensional blunt-body diameter D^*/D^*
d = diameter of the location of pressure measurement points
L = nondimensional spike length L^*/D^*
M = Mach number
p = nondimensional pressure $p^*/\rho_\infty^* u_\infty^{*2}$
p_{t2} = nondimensional pitot pressure
p_1 = nondimensional static pressure
Re = Reynolds number based on blunt-body diameter
Sr = Strouhal number, $f^* u_\infty^*/D^*$
t = nondimensional time $t^*(u_\infty^*/D^*)$
v = nondimensional velocity u^*/u_∞^*
α = angle of incidence, deg
β = shock angle, deg
Δp = pressure amplitude

Subscripts and Superscripts

∞ = freestream values
$*$ = dimensional quantities

Introduction

HIGH-SPEED spiked body flows or flows similar to them can appear in a variety of aerospace applications, such as axisymmetric jet inlets with conical centrebody,[1,2] ballistic missile drag reduction by spike,[3–6] plasma or hot-gas injection,[7] parachutes for pilot-ejection capsules,[8,9] or the ablation phenomenology associated with reentry problems.[10,11] It is well known that both steady and unsteady flows can appear over spiked body geometries depending on the spike length and the applied flow conditions. Although it was initially thought that the unsteady flow can occur in only one particular form,[3–5] it was soon found that in fact two very distinct unsteady flow modes can exist: oscillation and pulsation (with the terminology after Kabelitz[12]). Oscillation was characterized by

*Research Assistant, Department of Aerospace Engineering; currently Assistant Professor, Department of Mechanical and Aerospace Engineering, Carleton University, 1125 Colonel By Drive, Ottawa, Ontario K1S 5B6, Canada. Member AIAA.
†Senior Lecturer, Department of Aerospace Engineering. Member AIAA.
‡Mechan Professor, Department of Aerospace Engineering. Associate Fellow AIAA.
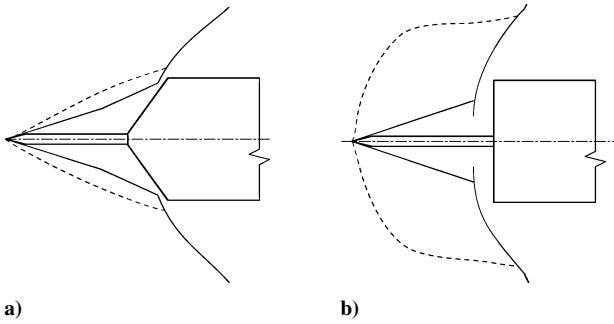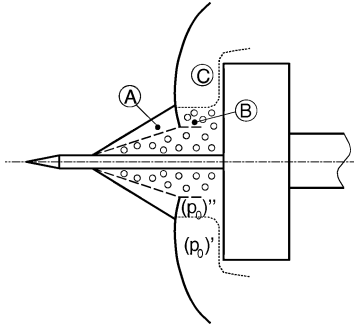
a change in the shape of the foreshock as it oscillates between a convex and a concave shape (Fig. 1a), whereas pulsation exhibits a somewhat more dramatic excursion between two very different shock envelopes (Fig. 1b).

The boundaries of the possible flow modes have been satisfactorily mapped for engineering purposes,[13–15] and it became well known that pulsation is typical of shorter spike lengths (between $L/D = 0.2$ and 1.5 for the particular geometry of this study) and oscillation of medium ones (from $L/D = 1.5$ to 2.5), whereas the flow becomes steady outside these ranges, that is, at very short or very long spikes. The driving mechanisms of the instabilities were also investigated by experimental means[3,5,15–18]; however, the various theories and hypotheses put forward are diverse with insufficient supporting evidence from the experiments. This is because of the difficulty of obtaining data from the flowfield at the high-speed freestreams considered (typically between Mach 2 and 10) and also because of the high frequency of the events (1000–7500 Hz) (Refs. 5 and 15).

Although computational fluid dynamics (CFD) can offer an alternative way of obtaining more data required for the analysis, it has not been utilized in detail for this purpose.[6,19,20] The objective of the present work was therefore to use CFD as a tool for the detailed investigation of the driving mechanisms of high-speed unsteady spiked body flows. Although a brief review of the overall research program, including the descriptions of pulsation, oscillation, and the transition between them, have been given in Ref. 21, the present paper will focus on the detailed analysis of the pulsation flow mode only.

Pulsation Theories

Various hypotheses have been suggested for the driving mechanism of pulsation in the past.[3,5,15–17] The first researcher dealing with this instability, although terming it as "oscillation," was Mair in 1952 (Ref. 3). Mair could not explain the origin of the unsteadiness, but he recognized the coexistence of a collapsing and a growing bow wave along the spike and also gave a thorough description of a complete cycle of pulsation. His most interesting finding concerned the observation of a vortex sheet at the intersection of the oblique foreshock and the normal bow wave in front of the blunt body and that of short duration high-speed expansion regions within the dead-air region.

In 1960 Maull[5] suggested that pulsation was driven by the pressure imbalance arising at the weak-shock/strong-shock intersection at the cylinder face, causing mass reversal into the conical dead-air region and leading to its inflation. He also observed the formation of the vortex sheet.

Antonov et al.[16] showed by using standard shock relations that the pressure behind the normal bow wave (p_0' in region C, Fig. 2) was

Fig. 1   Flow modes: a) oscillation and b) pulsation.

Fig. 2   Explanation of the pulsation mode according to Antonov et al.[16]

a)

b)

Fig. 3   Similarity between a) Edney's type IV shock formation[22] and b) the flowfield corresponding to the pulsation flow mode.[17]

actually smaller than that in region B (p_0'' in Fig. 2), and hence the mass influx into the dead-air region could not originate from region C, as suggested by Maull, but from region A behind the conical foreshock instead.

This idea was confirmed independently by Panaras,[17] who came up with probably the most original idea on the explanation of the flow reversal in pulsating flows: based on Edney's type IV shock envelope[22] (Fig. 3) he argued that a small supersonic jet curved toward the body axis will direct the flow from the region behind the conical foreshock into the dead-air region. He justified the supersonic nature of the jet by using quasi-steady shock hodographs, which were later modified by Kenworthy[15] to account for dynamic effects. According to these results, the flow should always be supersonic in region B (Fig. 2), regardless the freestream velocity.

Self-Sustained Oscillatory Flows

Unsteady spiked body flows can be put into context as a type of self-sustained oscillatory flows, according to the definition of Rockwell and Naudascher.[23] These highly organized oscillatory flows, which include instabilities such as cavity flows, jet-edge, jet-cylinder or jet-flap interactions etc., are sustained through a series of interacting events such as the production of organized disturbances at impingement; the feedback, or upstream propagation, of these disturbances from the impingement region to the area of separation of the free shear layer; the inducement of localized vorticity fluctuations at the separation caused by the arriving perturbations; and the amplification of these vorticity fluctuations in the shear layer between separation and impingement. Although all self-sustained oscillatory flows must incorporate these fundamental events, the flow features through which they are realized can differ for the various self-sustained oscillatiory flows. The identification of these elements in the unsteady spiked body flow of pulsation will also be the task of the present work.

Test Case

The test case to be analyzed was chosen from the experimental work of Kenworthy.[15] The model geometry was a forward-facing cylinder equipped with a spike of the length of $L/D = 1.00$ (Fig. 4). The freestream flow conditions were Mach 2.21 and $Re = 0.12 \times 10^6$. The flow was axisymmetric at zero angle of incidence. There were two pressure transducers placed at a diameter of $D/2$ on the face of the cylinder in the experiment, and the pressure was recorded at these points.
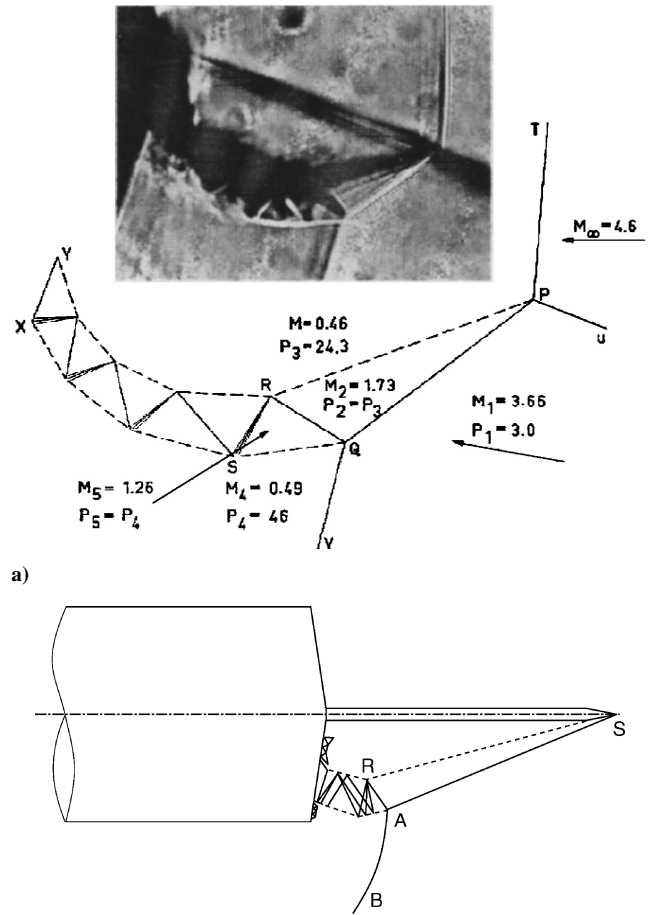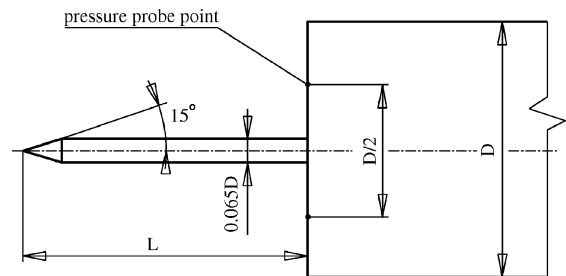

Fig. 4   Model geometry.

CFD Approach

Grid Generation

Because of the axisymmetry of the examined configuration, it was sufficient to model the body geometry in the two-dimensional plane. A structured, multiblock grid was generated, consisting of 160,000 cells in nine blocks. The first spacings near the wall (in both streamwise and cross-sectional directions) were of the value of $1.5 \times 10^{-4} \times D$. This grid will be referred to as the fine grid throughout this paper.

Numerical Method

The Parallel Multi-Block (PMB) code[24] was used for the numerical simulations. This is a generic CFD code developed at the University of Glasgow, employing a second-order cell-centered finite volume discretization method to solve the Navier–Stokes equations in two-dimensional, axisymmetric or three-dimensional fashion. In the present work, axisymmetric simulations were only performed, considering laminar flow conditions in the entire flowfield. Roe's

scheme, involving Harten's entropy fix[25] with MUSCL variable interpolation, was used to discretize the convective terms and central differencing for the diffusive ones, yielding a spatially second-order-accurate discretization scheme. Steady-state calculations proceed in two phases: the freestream starting solution is initially smoothed using an explicit scheme, and then an implicit scheme is employed to obtain rapid convergence. The linear system arising at each implicit time step is solved by using the generalized conjugate gradient method along with a BILU(0) factorisation as a preconditioner. An important feature of the code is the use of approximate Jacobian matrices for the left-hand side of the linear system. The unsteady part of the code is second-order accurate in time and employs an implicit unfactored dual-time method.

Results Verification

Three levels of grid density were considered for the grid-dependence tests. A medium and a coarse grid were extracted from the original fine mesh by taking every second and every fourth point in each direction, respectively. The result of this test is shown in Fig. 5, from which it can be seen that the three grid levels yield comparable time periods and pressure amplitudes. However, the coarse grid seems to miss some important features, such as the existence of a pressure plateau, the sharp pressure minima, and secondary peaks on the ascending and descending parts of the curve. The medium- and the fine-grid results show quite good similarity in these terms, and hence the medium grid appears sufficient.

The real time-step influence was also tested by decreasing the original, 0.0125, value by factors of 5 and 10, which comparison gave nearly identical pressure histories. Hence, the largest allowable time step can be considered for further analysis.

Results Validation

The computational results were validated in terms of the time-averaged pressure amplitudes Δp, the time-averaged Strouhal numbers Sr, the characteristic shape of the pressure traces and the shock envelope histories.

The evaluation of the time-averaged characteristics is given in Table 1, showing good agreement between experiment and CFD for both the pressure amplitude and the Strouhal number.

The characteristic shape of the pressure history, featuring a typical pressure plateau,[15] was also well captured by the numerical method and compares well with the sample curve available from the experiment (Fig. 6).

The experimental and numerical shock envelope histories are shown in Fig. 7. Note that the CFD results are presented in terms

Table 1 Comparison of the time averaged characteristics

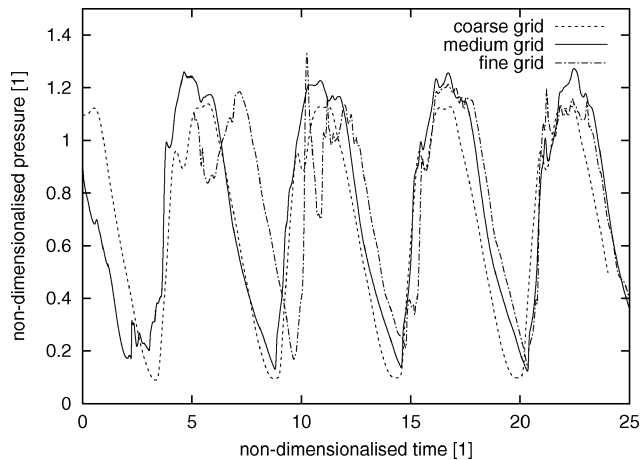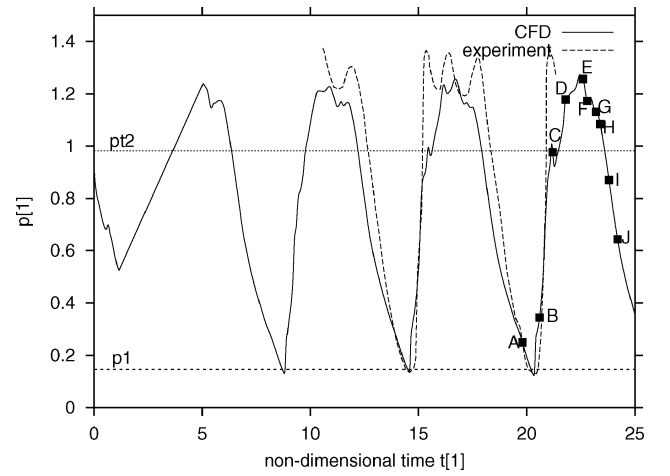| Method	Δp	Sr
Experiment[15]	1.1909	0.1725
CFD	1.1136	0.1727

Fig. 5 Grid-dependence test results.

Fig. 6 Comparison of the numerical and experimental pressure histories recorded on the cylinder face at the diameter of $d = D/2$.

of density isolines to allow comparison with the density gradients captured in the schlieren pictures. The time positioning of the CFD frames is indicated on the pressure trace of Fig. 6. In general, the agreement between the frames was found to be very good. The only discrepancies were observed in the extent of the expanding foreshock. In the experiment the foreshock remained attached to the spike tip at all times, whereas in CFD it is seen detached in frames A, I, and J (Figs. 6a, 6i, and 6j). However, as other flow features, such as the location of the foreshock-aftershock intersection or the general shape of the shock waves show good agreement with the experiment, it was concluded that the numerical results provide a credible account of the events occurring during pulsation and that they are well suited for further analysis.

Flow Conditions Behind Unsteady Shock Waves

To enable the analytical evaluation of the flow conditions during pulsation, exhibiting complex movements of shock waves, the following methodology has been developed.

Consider a flowfield characterised by a freestream Mach number of $M_\infty > 1$ and a normal shock wave moving downstream along the x axis with the velocity of v_x (Fig. 8).

Such flow can be interpreted in a co-ordinate system moving with a speed of v_x and featuring a standing shock wave. Then, the shock wave will be exposed not to the freestream Mach number M_∞, but instead to an effective one, M_e:

$$M_e = M_\infty - v_x/a_\infty = M_\infty - M_{x\infty} \quad (1)$$

This means that the flow Mach number upstream of the wave will be less than the actual freestream Mach number. Using standard shock relations,[26] the Mach number downstream of the moving shock wave M_2 can be evaluated as

$$M_2 = \sqrt{\frac{M_e^2 + 5}{7M_e^2 - 1}} \quad (2)$$

Note that this value is determined from M_e, and as such it represents the Mach number behind the shock wave, relative to the shock wave. To obtain the absolute Mach number M_{2A}, which is relative to a stationary point A (Fig. 8), M_2 has to be increased by v_x. However, because of the speed of sound a_2 being different behind the shock wave than the one in the freestream a_∞, M_{x2} behind the shock wave will also be different from $M_{x\infty}$ in front of it. M_{2A} should then be evaluated as

$$M_{2A} = M_2 + v_x/a_2 = M_2 + M_{x2} \quad (3)$$

where a_2 could be obtained from the following relation[26] (note that a_2 is based on the conditions corresponding to M_e and not M_∞):

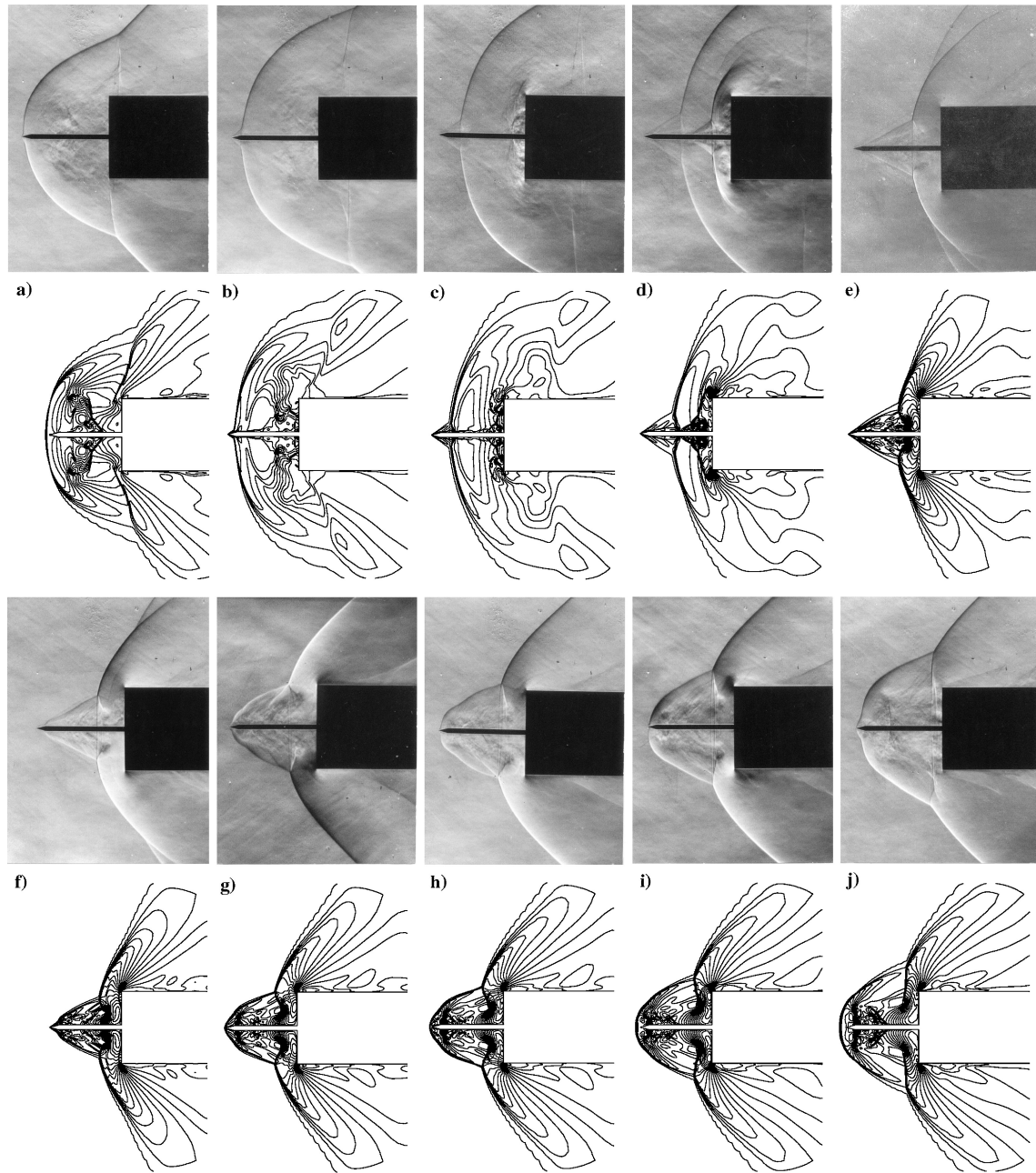$$\frac{a_2^2}{a_e^2} = \frac{(7M_e^2 - 1)(M_e^2 + 5)}{36M_e^2} \quad (4)$$

Fig. 7   Comparison of the schlieren pictures of Ref. 15 and the density isolines from the CFD for the frames indicated in Fig. 6.
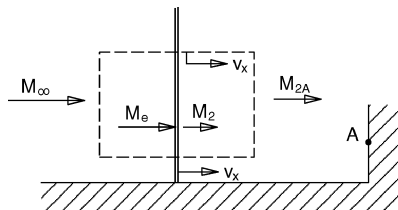

Fig. 8   Schematic of a moving normal shock wave.

Method of Analysis

The complexity of the flowfield dictates that for the purpose of analyzing the pulsation driving mechanism the number of frames per cycle used should be substantially larger than 10, the number typical for the experiments.[15,16,18] Therefore, from the CFD simulation 30 frames per cycle were used with three different types of flow visualizations presented simultaneously: the Mach-number isolines, which can reveal shear layers and boundary-layer separations; an

array of 10 instantaneous streamlines (numbered from the closest to the body axis outward), which also represent the local instantaneous flow-path directions and which are shown superimposed on the Mach contour plots, and pressure isolines, which enable the identification of shock waves and vortices. Extra streamlines and detailed vector plots are also shown when necessary to explain interesting phenomena.

Analysis of CFD Results

The sequence of 30 flow-visualization frames is shown in Fig. 9. The nondimensional time difference between each of these frames was $\Delta t = 0.2$, with the pointtiming of the frames indicated in Fig. 10.

To identify the dominant movements of the shock system and to allow analytical evaluations, a reference point relating to the shock envelope was selected. Following Zapriagaev and Mironov,[18] the triple point (corresponding to the foreshock-aftershock intersection) proved to be the best choice for this purpose, because this incorporates both the longitudinal movement as well as the lateral expansion

of the bow wave. The position of this reference point in time was tracked and plotted in Fig. 11a, while the temporal variation of the foreshock angle at the triple point was evaluated in Fig. 11b. The origin of the coordinate system for these plots was set to the center of the afterbody face. The triple point was monitored only while in the region of interest, that is, in front of the cylinder face. For some of the cycle, there were two triple points present, one in the collapsing shock system and another in the growing one. After the two merged, the second triple point disappeared.

Based on these graphs and the frame sequence, it was found useful to divide the pulsation cycle into three main sections (with the frame numbers from Fig. 9): 1) collapse (frames 1–9), for which the rapid horizontal movement of the reference point is characteristic; 2) inflation (frames 10–20), for which the fast lateral movement of the foreshock-aftershock intersection is dominant; and 3) withhold (frames 21–30), during which the expanded foreshock is almost stationary.

Because of the numerous flow features emerging and dispersing during these events, flow schematics helping their identification were created in Figs. 12–15 in which shock waves were noted as W, separated regions as P, shear layers as L, and vortical regions as V. They were numbered in the order of their appearance duing the pulsation cycle.

Process of Collapse: Frames 1–9

In frame 1 (Fig. 9) bow wave W2 (Fig. 12) has already accomplished its expansion and starts to migrate toward the afterbody. The minimum pressure on the cylinder face has just been passed (Fig. 10)
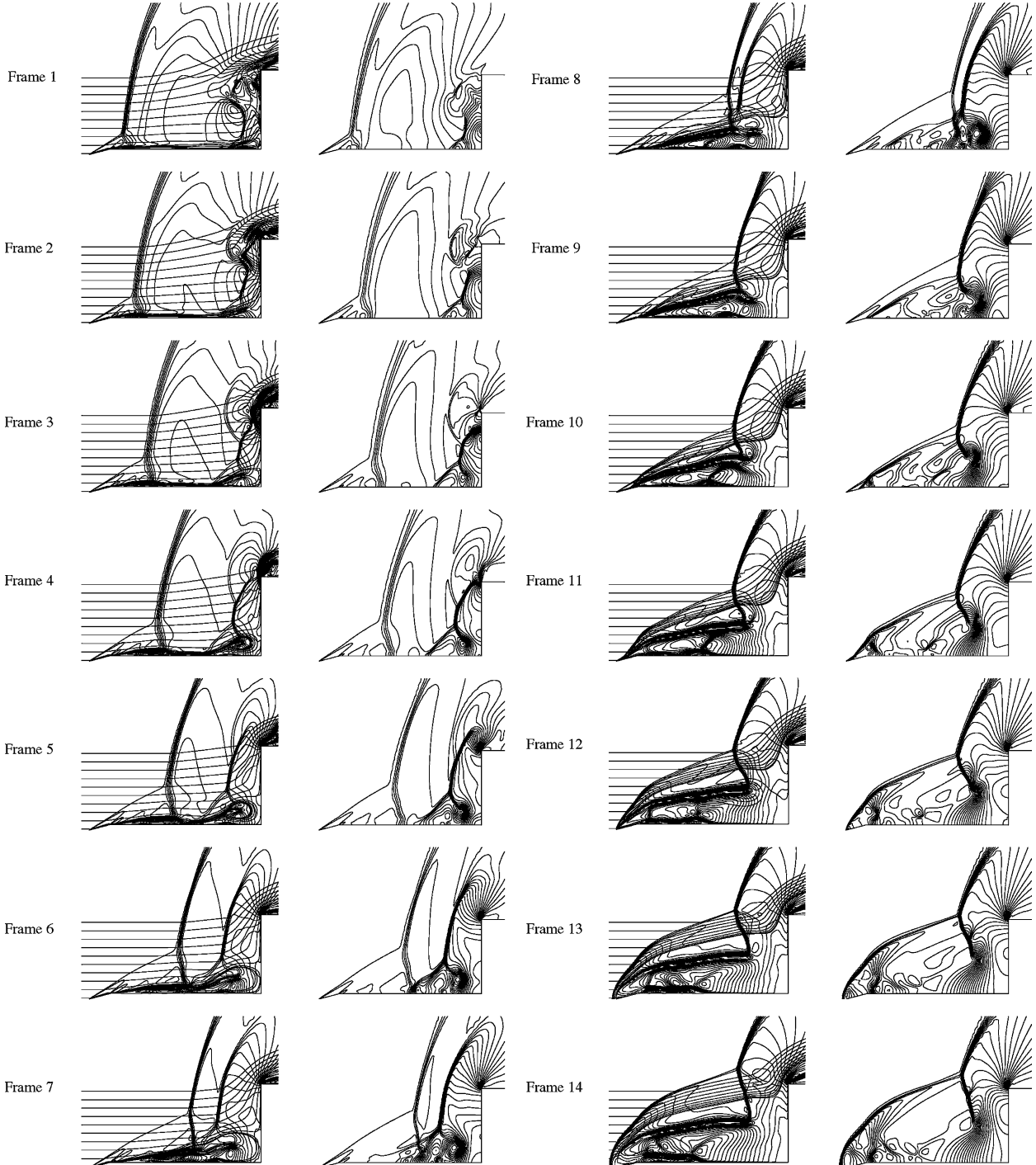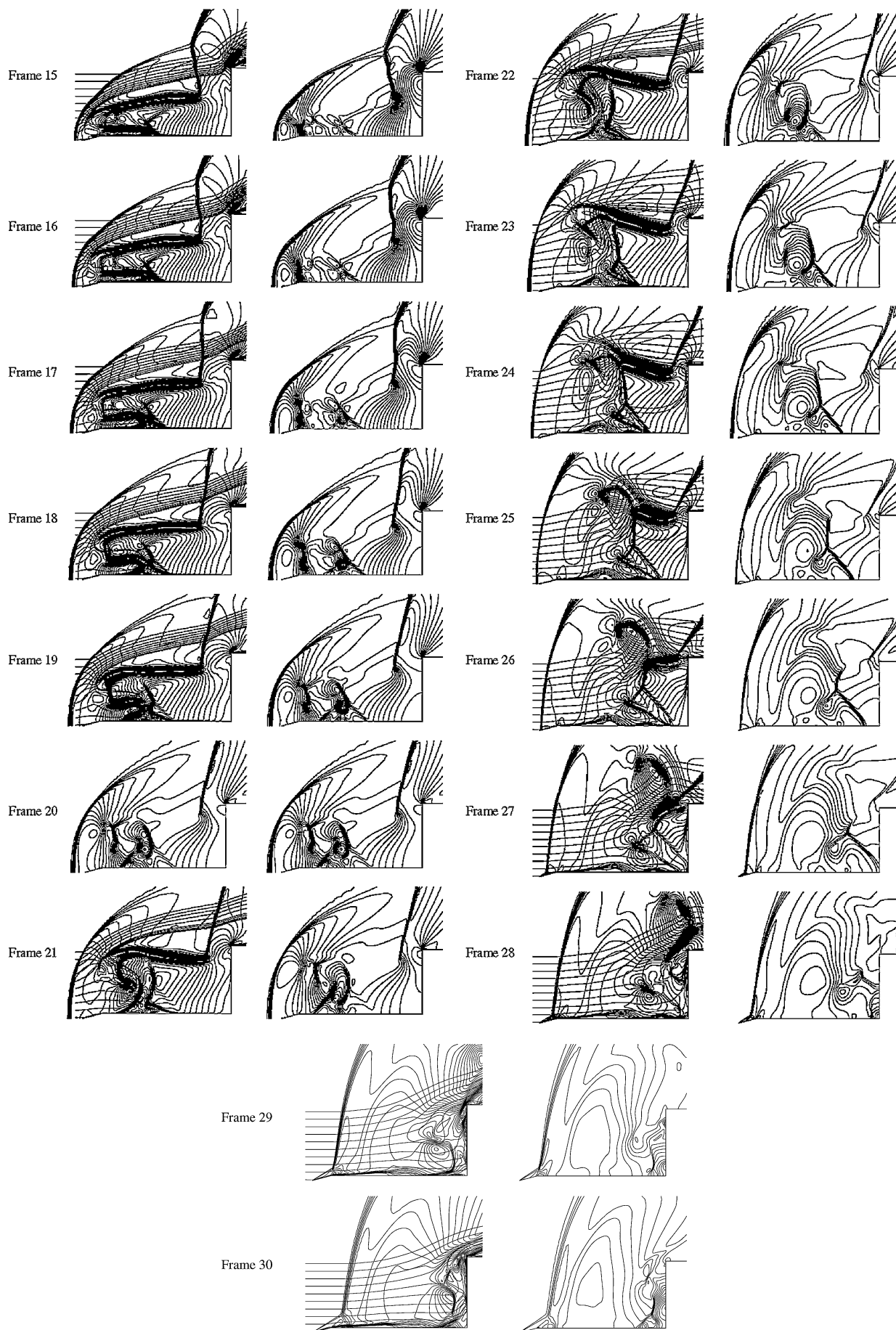

Fig. 9   Pulsation at Mach 2.21, $L/D = 1.00$. Shown are the Mach isolines superimposed with instantaneous streamlines (left column) and the pressure isolines (right column).

Fig. 9 Pulsation at Mach 2.21, *L/D* = 1.00. Shown are the Mach isolines superimposed with instantaneous streamlines (left column) and the pressure isolines (right column) (continued).
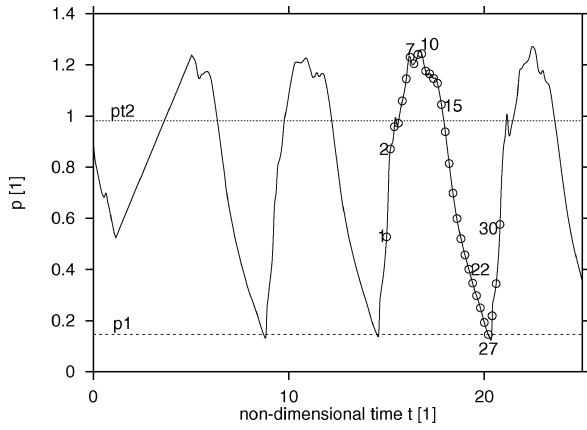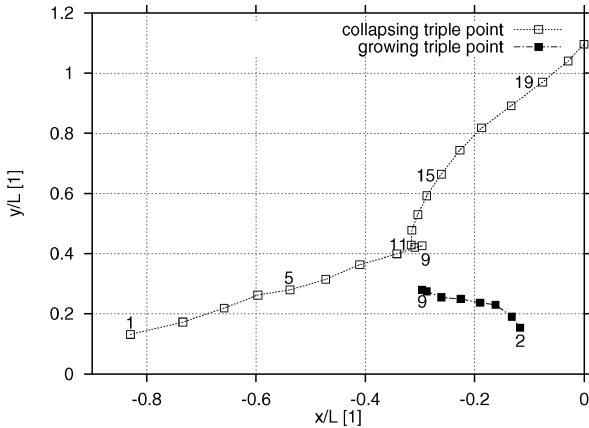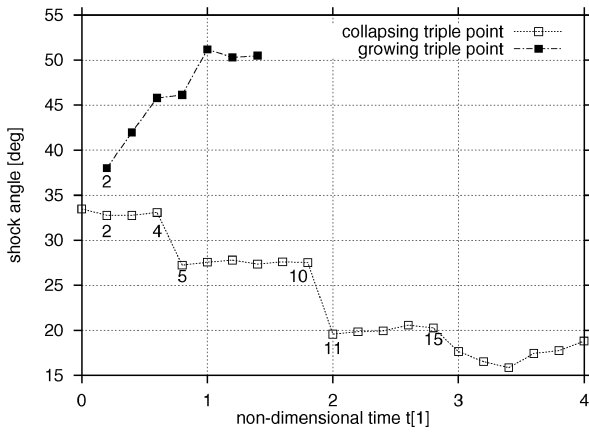
Fig. 10 Pressure history at the cylinder face ($d = D/2$) for the Mach 2.21 pulsation case.

and begins to rise as shock W2 moves downstream. As the most forward portion of the spike becomes exposed to supersonic freestream, an oblique conical foreshock W1 will emanate from the spike tip. This intersects bow wave W2. The angle of W1 is 33 deg (Fig. 11b), which is basically the value expected for a 15-deg semivertex cone angle[26] represented by the spike tip. The flow behind W1 is supersonic and is decelerated through another oblique shock wave W3, emanating from the triple point T1 to comply with the subsonic flow behind W2. As this oblique wave interacts with the boundary layer on the spike, a separated region P1 is formed. The first sign of this is visible in frame 1 and is further developed in frame 2.

The speed of the collapsing bow wave appears to be very nearly constant between frames 1–9 (Fig. 11a), and it can be determined as

$$v_x = (x_9 - x_1)/(t_9 - t_1) = 0.3335$$

According to Eq. (2), $M_{x\infty}$ will be 0.737, and the effective Mach number acting on shock W2

$$M_e = M_\infty - M_{x\infty} = 2.21 - 0.737 = 1.473$$

Using Eq. (2), M_2 (based on M_e) can be evaluated as $M_2 = 0.711$. This is the relative Mach number behind the shock wave. The
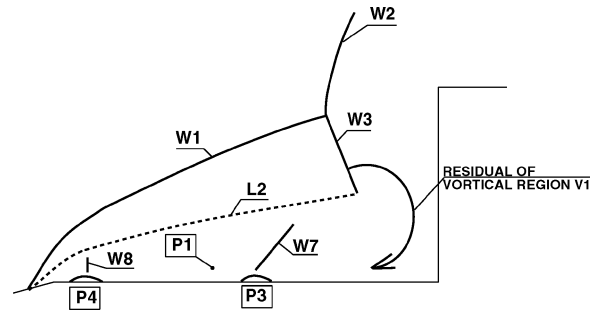

Fig. 13 Scheme of the shock system during the final phase of collapse and initial phase of inflation (based on frames 10/11).
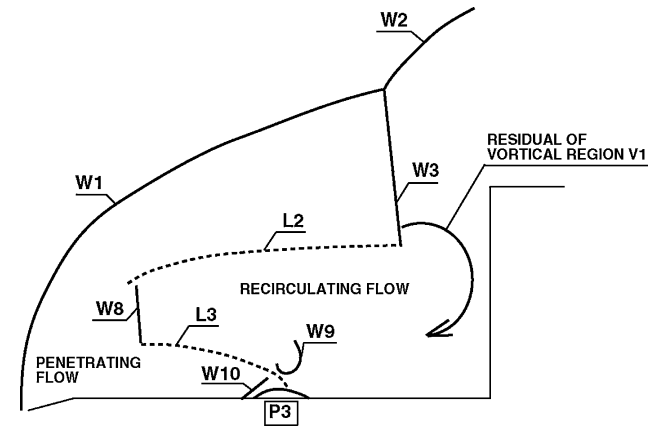

a)

b)

Fig. 11 Variation of a) the triple point location and b) the foreshock angle during pulsation with the frame numbers indicated.

Fig. 14 Scheme of the shock system during the late phase of inflation and initial phase of withhold (based on frames 18/19).

a)   b)

Fig. 12 Scheme of the shock system during collapse (based on frames 3/4).
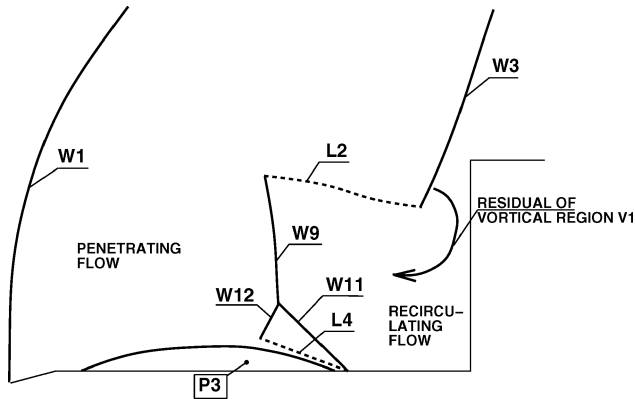
Fig. 15 Scheme of the shock system during the late phase of withold and initial phase of collapse (based on frames 24/26).
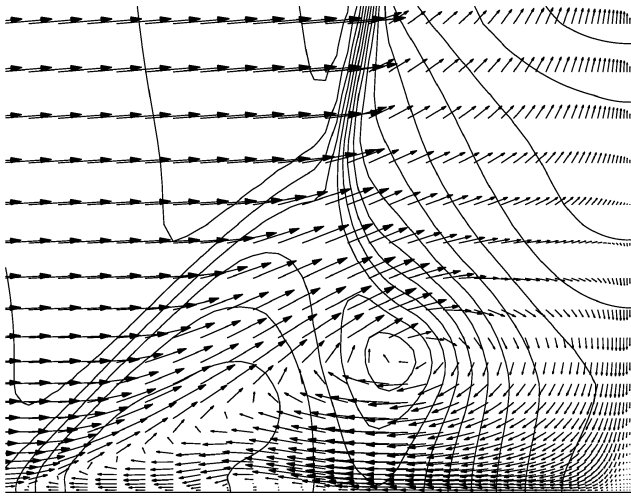

Fig. 16 Vector plot detail and pressure isolines for frame 3 from Fig. 9, Mach 2.21 freestream (every second vector shown only).

absolute Mach number relative to the body can then be obtained from Eqs. (3) and (4) as

$$M_{2A} = M_2 + M_{x2} = 0.711 + 0.646 = 1.357$$

This agrees well with the value predicted by the numerical simulation, and it means that although the afterbody is in the wake of a normal wave it is still exposed to a supersonic stream. Hence, a new normal shock W5 is created in front of the cylinder face, which first sign is visible in frame 1 (Fig. 9). This new bow wave interacts with the boundary layer on the spike and creates another separation P2. The first (i.e., lowest) shown streamline entering the shock system is seen to be reversed by the cylinder face resulting in separation point P2 being induced forward (frame 2).

By frame 2 separation region P1 has grown downstream, tracking the collapsing bow wave. P2, on the other hand, has moved farther forward ahead of the growing bow wave W5, generating a weak oblique shock W4. As W4 intersects W5, another triple shock system similar to the one at the spike tip is formed (T2, W6). In frames 3 and 4 the two separated regions P1 and P2 gradually grow and move closer to each other while the secondary triple shock system becomes more clearly developed.

As a consequence of this, a shear layer L1 is formed on the boundary of separation zone P2 and the supersonic region behind shock wave W4 (Fig. 12 and frame 2). Assuming a zero pressure gradient through the shear layer, $\partial p/\partial y = 0$, the pressures in these two regions will be equal and relatively low ($p_A = p_D$; see Fig. 12b). However, the pressure behind shock W6 (p_C) will be high because

it will tend to equal the high pressure arising behind the normal wave W5 ($p_B = p_C$). Thus, the pressure imbalance between p_C and p_D will lead to a strong favorable pressure gradient of clockwise direction into the separation zone. As this flow is immediately reversed through shear layer L1 (Fig. 16), a significant vortical region V1 is formed at the bottom of shock W6. The vortical region can be clearly recognized in the pressure plot of frame 3, characterized by concentric, nearly circular isolines and a low pressure in the center. This is the vortex sheet observed by Mair,[3] Maull,[5] and Ferri and Nucci[27] and is the key to the pulsation driving mechanism. It can also be identified as the fundamental element of the self-sustained oscillatory flow representing the organized disturbance at impingement.[23] In accordance with the experimental observation,[5] this vortical region exists for a very short period of time only, approximately $\frac{1}{6}$th of the instability cycle.

The primary effect of the vortical region V1 is the flow reversal of the lowest streamlines, such as streamline 1, into the separation zone, from where it reverses and reenters the supersonic zone (behind foreshock W4) through shear layer L1. The filling effect intensifies with time as the next introduced streamline becomes involved in this process in frame 4. The introduced streamlines outside these, although being deflected downward from their original direction, reach the face at an angle larger than zero and hence eventually flow outward.

The pressure gradient created by V1 also affects the spike boundary layer. The clockwise pressure gradient is in fact a favorable gradient on the downstream side of V1, thinning the boundary layer there (see the vector plot detail of frame 3, Fig. 16). However, it creates an adverse pressure gradient on the upstream side of vortex V1, resulting in a thickening effect and eventually the separation of the boundary layer there (Fig. 16). Thus, a new separated region P3 of reverse direction to P1 and P2 and embedded in the latter one appears just in front of V1 (see Fig. 12 and frame 2). It will be shown later that P3 is maintained and grows for almost the entire pulsation cycle and, similar to the vortical region V1, is a key to the driving mechanism of pulsation.

By frames 4 and 5 the primary shock system, W1-W2-W3, is seen to continue its migration downstream as the secondary one, W4-W5-W6, gradually strengthens. This leads to the growth of vortical region V1 and the enlargement of separated region P3. Note that the position of P3 remains stationary and connected to V1.

By frames 6 and 7 separation regions P1 and P2 merge to form an enlarged region that we will call P1 with a resultant merged shear layer L2 (Fig. 13). This event creates an enlargened zone for the reversed high pressure flow to fill. The separation point of P1 remains stationary during this period until frame 7. The induced flowfield of the vortical region and associated pressure gradient is sufficient for the reversed flow to achieve supersonic speeds locally (around Mach 2). This is the explanation of the strong expansion region captured by Mair[3] in 1952.

Also during this period the angle of W1 drops rapidly from 33 to 27 deg (frames 5,6,7 in Fig. 11b). This is caused by the expansion waves emanating from the spike tip shoulder weakening the foreshock. The shock wave angle of 27 deg corresponds to the Mach line at the Mach 2.21 freestream.[26] The flow thus has zero deflection through the oblique shock wave W1, which is indeed the case in flow visualization frames 5, 6, and 7.

By frame 8 the secondary foreshock (W4) has almost disappeared as the growing shock system starts to merge with the collapsing one. Although the vortical region remains active and continues to reverse the flow in the separation zone, this process no longer involves flow originating directly from the freestream.

This important finding means that the whole of the forthcoming inflation of the dead-air region is not caused by a mass influx, as previously thought, but because of the expansion of the high-pressure gas (generally above p_{t2}; see Fig. 10) already trapped in this zone. Thus, the hypotheses of Antonov et al.,[16] Panaras,[17] and Kenworthy[15] regarding the continuous filling of the separation region throughout the entire duration of inflation, for example, through Edney's jet, has to be reformulated according to these new findings.

At this stage the very first point of separation zone P1 has still not advanced, and the reversed flow is impeded by the oncoming

pressure wave associated with the first triple shock. In frame 9 the two bow waves merge. The position where they meet corresponds to the shock-detachment distance of the blunt body in the freestream. This is explained by the collapsing bow shock (W1) becoming sufficiently weak to have little effect on the flowfield at this stage. Thus the growing bow shock (W5) is then fully exposed to freestream conditions.

The most important feature of frame 9, however, concerns the behavior of the vortical region itself. The oncoming pressure wave passes through the region to leave a strong favorable upstream pressure gradient. This process can be closely observed in the vector plots of Figs. 17 and 18, showing also how separation region P3 is affected. With the sudden lack of the adverse pressure gradient, the fluid within the boundary layer is now accelerated in the upstream direction, slowing the flow reversal.

The axial velocity of the triple point becomes suddenly very small at this moment ($v_x = 0$, and thus $M_{x\infty} = M_{x2} = 0$, as shown in Fig. 11a), which leads to an instant drop of the Mach number behind the shock wave from supersonic, $M = 1.473$, to a fully subsonic value. Another interpretation of this situation is that the resulting normal shock adopts a position as though it were the growing bow wave.

Note that by frame 9 the most forward separation point P1 finally starts to move forward toward the spike tip. This is associated with the maximum pressure recorded at the cylinder face (Fig. 10), which maximizes the flow escape to forward within the dead-air region.
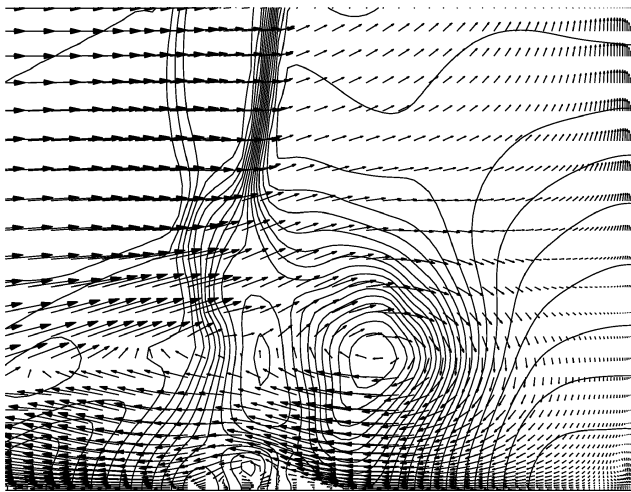
Process of Inflation: Frames 10–20

Frame 10 shows the beginning of the lateral expansion of the foreshock. The lowest part of shock W3 has just reached its most rearward position because of the dynamics of the collapse.

This unique shape means that W3 will act as a weak oblique shock on the lowest streamlines involved in the recirculation (see the sketch in Fig. 13), and thus a supersonic pocket characterized by Mach numbers around 1.2 will appear behind shock W3 for a short period of time (frame 10 only). This zone was fully subsonic before. The pressure field of the residual of vortical region V1 starts to enlarge and weaken as the high-pressure gas accumulated at the cylinder face (the pressure reaches its maximum in frames 9 and 10) escapes upstream with supersonic speeds. This is the only possible path of flow as the direction of the pressure field does not allow any other solution. The growing region of the pressure gradient will also move separation point P3 upstream, which, as a result of this effect, will alter to a locally thickened boundary layer. This causes the highly accelerated flow represented by Mach numbers as high as 2 to be channelled over it through a weak oblique shock W7 (Fig. 13), which is apparent from the pressure isolines of frame 10. This in turn interacts with the locally thickened boundary layer and separates it again (see the vector plot of frame 10, Fig. 19). This is an important feature because although P3 will play a role later it could have disappeared without the revitalizing effect of W7.

As the recirculated gas reenters the supersonic region behind W1 through shear layer L2, it collides with the flow originating from the freestream. This results in the flow being recirculated again and reenergized by the outer flow. This effect is visualized in frame 12 by introducing an additional streamline originated near the bottom part of shock W3.

This demonstrates that the expansion process is internally fed, rather than originating from outside. It means that the resulting flow recirculation enables the high-pressure gas accumulated at the cylinder face during the collapse to expand upstream into the separation zone. As a consequence of this, separation point P1 advances from the spike shoulder toward the tip. The shear layer originating from it (L2) seems however to keep the same angle relative to the spike surface, so that when the spike tip shoulder is passed (frame 11) a break in the shape of the shear layer appears.

It is interesting to examine the angle of the foreshock at the triple point at this time instant. It takes on a value of 20 deg (Fig. 11b), which could not exist normally in a freestream of Mach 2.21 (Ref. 26). The Mach angle at this speed is 27 deg, which suggests that another factor has to be taken into account. According to Fig. 11b, the sudden drop from 27 to 20 deg happens at frame 11, and this is the value preserved then through the next four frames. These correspond to the period when the triple point starts to move laterally outward.

By adding the Mach number arising from the lateral movement to that of the freestream flow, a new resultant flow can be obtained,

Fig. 17   Vector plot detail and pressure isolines for frame 8 from Fig. 9, Mach 2.21 freestream (every second vector shown only).

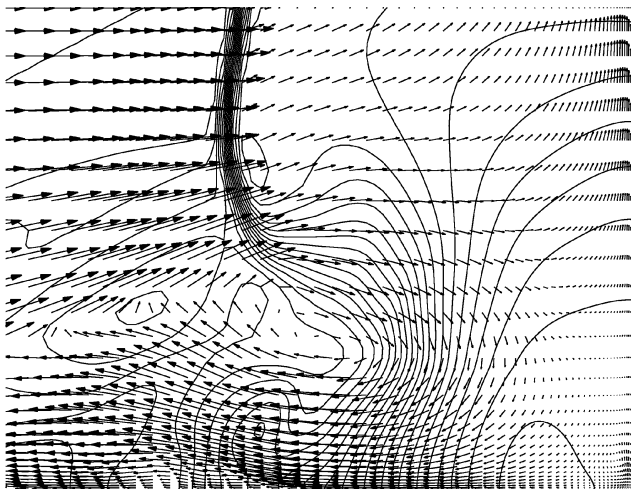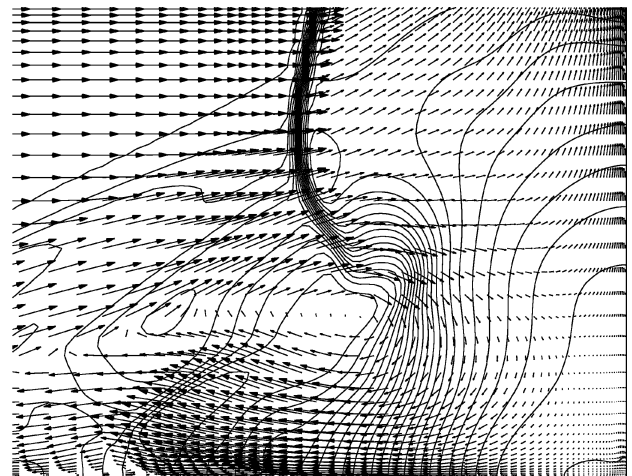**Fig. 18   Vector plot detail and pressure isolines for frame 9 from Fig. 9, Mach 2.21 freestream (every second vector shown only).**

Fig. 19   Vector plot detail and pressure isolines for frame 10 from Fig. 9, Mach 2.21 freestream (every second vector shown only).

which Mach number will be

$$M_e = \sqrt{M_\infty^2 + M_{y\infty}^2} = 2.28$$

acting at an angle of $\alpha = 14.1$ deg. Now, the effective angle between the foreshock and the resultant flow will be

$$\beta_e = \beta + \alpha = 20 \text{ deg} + 14.1 \text{ deg} = 34.1 \text{ deg}$$

These conditions (upstream Mach number 2.28, shock angle 34.1 deg) result in a Mach number behind the foreshock of 1.89 and a deflection of 10.2 deg, which are again in good agreement with the CFD results, yielding 1.92 for the Mach number and 10.1 deg for the deflection. (Note that the deflection is measured from the freestream direction.) This analysis confirms Kenworthy's suggestion[15] that shock systems during the pulsation mode should be considered as unsteady instead of quasi-steady.

By frames 11 and 12 separation point P1 reaches the spike tip, and the recirculation zone starts to expand laterally. This will have a dual effect. First, the cross-sectional area at P3 will increase, leading to the disappearance of shock W7 (frames 11 and 12). Second, the angle of foreshock W1 near the spike tip will also grow, and thus W1 itself will strengthen (frames 13 and 14). This will yield an increase in the pressure behind the shock so the recirculated supersonic flow has to be decelerated to these conditions before reentering shear layer L2. Hence, an internal normal bow wave W8 is generated in the vicinity of the spike tip shoulder (frames 11 and 12 and also Fig. 13), and as it interacts with the boundary layer yet another separation P4; embedded in the recirculation zone, occurs.

Frame 13 marks the first time instant of foreshock W1 becoming normal near the center line as it detaches from the spike tip. This means the creation of a sizeable high-pressure region behind this bow wave, causing shear layer L2 to be lifted off from the spike tip. The first introduced streamline is thus able to penetrate more deeply below the separation zone, absorbing P4 and even reaching the location of the other internal separated region P3 (the resultant of the two will be called as P3) and creating another shear layer L3 originating from it (frames 13–16 and Fig. 14). It is interesting to follow the path of this streamline: it enters the recirculation region via shear layer L3, turns back to a direction opposite to the freestream (see the vector plot detail of frame 14 in Fig. 20), then enters the supersonic flowfield behind the oblique portion of W1 through the internal normal wave W8, and finally passes the afterbody shoulder via the triple shock system. Also note that as shear layer L2 moves away from the center, the triple point is gradually displaced in the lateral direction.

By frame 17 the second introduced streamline joins the first one in passing below the newly formed shear layer L3. A high-pressure pocket can be observed at around the half spike length (or the location of the separation point of P3), which appears as a result of
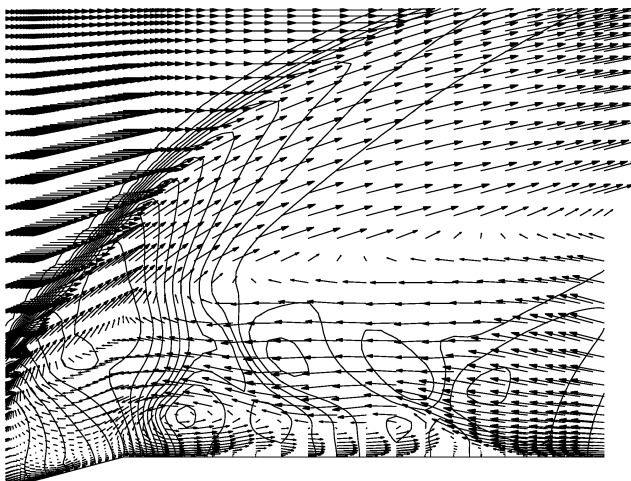

Fig. 20 Vector plot detail and pressure isolines for frame 14 from Fig. 9, Mach 2.21 freestream (every second vector shown only).
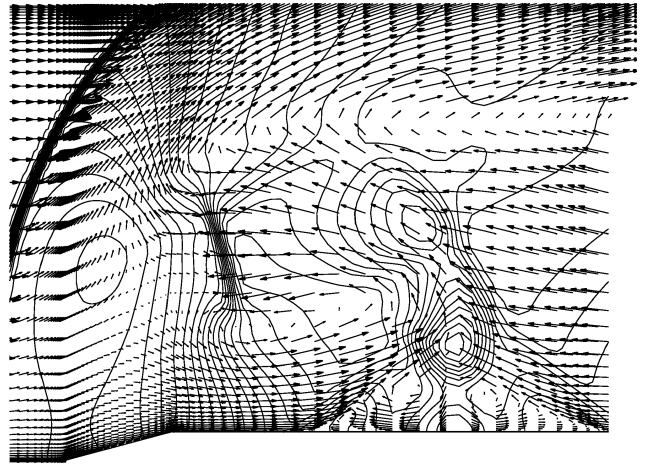

Fig. 21 Vector plot detail and pressure isolines for frame 19 from Fig. 9, Mach 2.21 freestream (every second vector shown only).

the collision of the penetrating and recirculating streams as they are almost brought to a standstill there. The first sign of the pocket actually appears two frames earlier, on frame 15, and it gradually grows until frame 22. Because it is created in a relatively low-pressure environment, it will be surrounded by a curved shock wave W9 (frames 17–20 and Fig. 14). The collision of the flows is well illustrated in the vector plot detail of frame 19, Fig. 21.

Another interesting feature apparent from this figure is the effect of shock W8 on the penetrating flow. Because shock W8 determines the direction of the pressure gradient locally (high to low in a downstream direction), the same gradient will act as an expansion ray on the penetrating flow as well. Hence, it will experience an expansion from high pressure to low pressure, strong enough to accelerate it to supersonic speed (Mach 1.8) before colliding with the recirculated flow (frame 19).

By frames 18–20 the number of the introduced streamlines participating in this penetration process increases to three, causing a continuing liftoff of shear layer L3. Shock W8 moves downstream, rotates and also moves radially outward because of the high pressure behind the expanded foreshock W1 and also because of the shifting shear layer L3. It also weakens with little evidence of it by frame 24.

For a short period of time (frames 19–21), an oblique wave W10 appears in front of the high-pressure pocket, because separation region P3 has been so enlarged that it will dictate large flow deflections.

The preceding observations are original in that sense that they reveal a new path for the flow entering the recirculation zone through the expanded bow wave. Although previous researchers[15−17] believed that this flow reaches the afterbody face in a straightforward manner before passing the cylinder shoulder, it has been shown in the present work that it is actually turned back against the freestream via shear layer L3 to enter the supersonic conical flow region behind the expanded foreshock before passing the afterbody shoulder. The more flow becomes involved in this process, the larger the normal portion of the foreshock becomes (frames 18–22). This enables the volume dominated by high-pressure gas (generated by the normal shock) to greatly grow in the vicinity of the spike tip.

Withhold: Frames 21–30

Frames 21 and 22 mark the most forward position of bow wave W1, and even when it starts to move downstream in frame 23 it continues to expand laterally (frames 23–25). This justifies the use of term "withold" for this section. During this process, shock W1 transforms from a combined normal and oblique shock to a predominantly normal bow wave (frames 25–30).

The withhold and the actual lateral expansion occurs because of the equilibrium between the high-pressure zone behind foreshock W1 and the low-pressure recirculation zone. These two are separated by shock wave W9 (frames 23–25); however, because of the liftoff of the primary shear layer L2 the size of the high-pressure
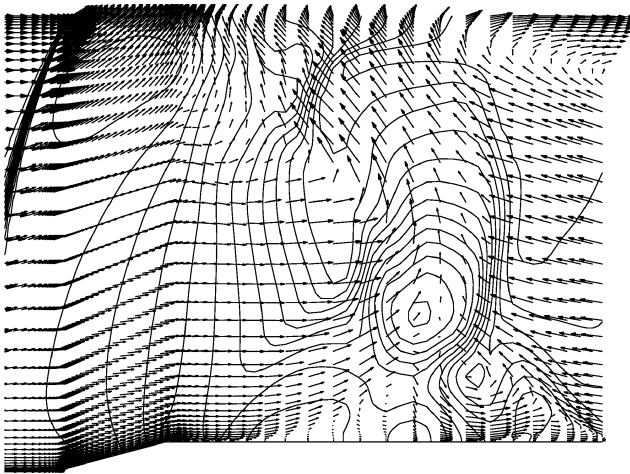
Fig. 22   Vector plot detail and pressure isolines for frame 22 from Fig. 9, Mach 2.21 freestream (every second vector shown only).
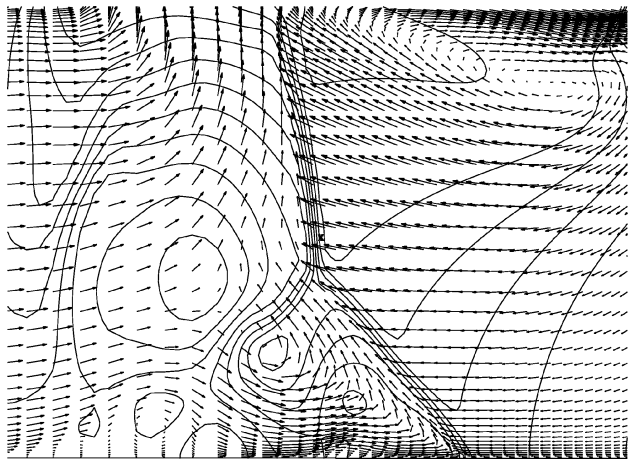

Fig. 23   Vector plot detail and pressure isolines for frame 24 from Fig. 9, Mach 2.21 freestream (every second vector shown only).

subsonic region will gradually grow until it prevails the effect of the lower-pressure recirculation zone (frame 25). Hence, the expanded shock system is seen to collapse in frames 25–30. It is true that for a short time (frames 25 and 26) the mass influx into the collapsing separation zone is renewed through as many as four of the introduced streamlines; it is able only to delay the ongoing processes but not to reverse them. When this feature disappears, the collapse suddenly accelerates, and a new cycle starts again in frame 30, which is identical to frame 1.

An interesting feature of the withhold section is that another triple shock system, the third during a single pulsation cycle, appears inside the separation region. Its normal shock portion is formed from the originally curved W9 shock, which has gradually opened as the number of penetrating streamlines increased. By this, the extent of the collision has also grown, which is well demonstrated on the vector plot details of frames 22 and 24 (Figs. 22 and 23). The deflection of the recirculated flow in these frames appear to be nearly 90 deg, which would be a nonexistent solution from the shock-wave theory.[26] This further substantiates that W9 is a shock wave indeed induced by only a need for a boundary between two very different flow states.

In frame 27 the pressure on the face reaches its lowest point and is then approximately equal to the freestream static pressure (see Fig. 10).

Hypersonic Considerations

A similar simulation and analysis was performed for the $L/D = 1.00$ spiked cylinder at Mach 6.00, $Re = 0.13 \times 10^6$

freestream too.[28,29] It was found that the pulsation mechanism appearing in this case was identical to the one in the supersonic freestream, apart from some small differences in the shape of the shock envelope. These were caused by the increased freestream velocity and meant a generally lower foreshock angle caused by the higher freestream as well as the foreshock-aftershock intersection lying closer to the afterbody. All of these effects resulted in a more bell-like shape of the expanded foreshock. In general, however, the just-described pulsation mechanism was found to be Mach-number independent, valid for both supersonic and hypersonic freestreams. For full details, see Ref. 29.

Conclusions

The driving mechanism of the pulsation flow mode arising over axisymmetric spiked bodies has been analyzed by using CFD as a tool. Previous pulsation hypotheses have been extended and modified by revealing a number of new key elements in the driving mechanism. These concerned the creation of a vortical region at the foreshock-aftershock intersection causing the filling of the dead-air region, the liftoff of the shear layer from the spike tip once a bow wave was created there, the penetration of the flow below the shear layer until about the half spike length and its consequent turn back against the freestream, and finally the existence of two different regions during the withold and collapse of the expanded foreshock. Other important observations regarded the duration of the mass influx into the dead-air region: it was found to last only for the $\frac{1}{6}$ of the total time period of the pulsation cycle and meant that the inflation of the shock system was caused by the expansion of this nearly constant volume gas rather than by a continuous mass influx as previously believed.

The vortex sheet can be understood as an organized disturbance at impingement in the theory of self-sustained oscillatory flows,[23] which also serves as the source for upstream propagating signals in the dead-air region.

References

[1]Oswatitsch, K., "Der Druckrückgewinn bei Geschossen mit Rückstossantrieb bei Hohen Überschallgeschwindigkeiten," Bericht Nr 1005, Forch. & Entwickl. Heereswaffenamtes and NACA TM 1140, 1944.

[2]Lu, P., and Jain, L., "Numerical Investigation of Inlet Buzz," *Journal of Propulsion and Power*, Vol. 14, No. 1, 1998, pp. 90–99.

[3]Mair, W., "Experiments on Separation of Boundary Layer on Probes in Front of Blunt Nosed Bodies in a Supersonic Stream," *Philosophical Magazine*, Vol. 43, No. 342, July 1952, pp. 593–601.

[4]Bogdonoff, S., and Vas, I., "Preliminary Investigations of Spiked Bodies at Hypersonic Speeds," *Journal of the Aerospace Sciences*, Vol. 26, No. 2, 1959, pp. 65–74.

[5]Maull, D. J., "Hypersonic Flow over Axially Symmetric Spiked Bodies," *Journal of Fluid Mechanics*, Vol. 8, 1994, pp. 584–592.

[6]Yamauchi, M., and Fujii, K., and Highashino, F., "Numerical Investigation of Supersonic Flows Around Spiked Blunt Body," *Journal of Spacecraft and Rockets*, Vol. 32, No. 1, 1995, pp. 32–42.

[7]Ganiev, Y., Gordeev, V., Krasilnikov, A., Lagutin, V., Otmennikov, V., and Panasenko, A., "Aerodynamic Drag Reduction by Plasma and Hot-Gas Injection," *Journal of Thermophysics and Heat Transfer*, Vol. 14, No. 1, 2000, pp. 10–17.

[8]Roberts, B., "An Experimental Study of the Drag of Rigid Models Representing Two Parachute Designs at $M = 1.40$ and 2.19," Royal Aircraft Establishment, TN Aero 2734, 1960.

[9]Maynard, J., "Aerodynamic Characteristics of Parachutes at Mach Numbers 1.6 to 3.0," NASA TN D 752, 1961.

[10]Minges, M., "Ablation Phenomenology (a Review)," *High Temperatures—High Pressures*, Vol. 1, No. 6, 1969, pp. 607–649.

[11]Abbett, M., Cooper, L., Dahm, T., and Jackson, M., "Flow Characteristics About Concave Conic Forebodies at High Mach Numbers," AIAA Paper 75-153, 1975; also *AIAA Journal*, Vol. 13, No. 11, 1975, pp. 1419, 1420.

[12]Kabelitz, H., "Zur Stabilität Geschlossener Greznschichtablösegebeite an Konischen Drehkörpern bei Hyperschallströmung," DLR, FB: 71-77, Germany, 1971.

[13]Wood, C., "Hypersonic Flow Over Spiked Cones," *Journal of Fluid Mechanics*, Vol. 12, No. 4, 1961, pp. 614–624.

[14]Holden, M., "Experimental Studies of Separated Flows at Hypersonic Speeds. Part I—Separated Flows over Axisymmetric Spiked Bodies," *AIAA Journal*, Vol. 4, No. 4, 1966, pp. 22, 23.

[15]Kenworthy, M., "A Study of Unstable Axisymmetric Separation in High Speed Flows," Ph.D. Dissertation, Dept. of Aerospace and Ocean Engineering, Virginia Polytechnic Inst. and State Univ., Blacksburg, VA, 1978.

[16]Antonov, A., and Gretsov, V., and Shalaev, S., "Experimental Investigation of the Characteristics of Unsteady Separated Regions Arising in the Supersonic Flow at a Spiked Body," *Zhurnal Prikladnoi Mekhaniki i Tekhnicheskoi Fiziki*, Aug. 1976, pp. 118–124.

[17]Panaras, A., "Pulsating Flows About Axisymmetric Concave Bodies," *AIAA Journal*, Vol. 19, No. 6, 1981, pp. 804–806.

[18]Zapriagaev, V., and Mironov, S., "An Experimental Study of Fluctuations in the Front Separation Zone at Supersonic Flow Velocities," *Zhurnal Prikladnoi Mekhaniki i Tekhnicheskoi Fiziki*, Aug. 1989, pp. 116–124.

[19]Shang, J., and Hankey, W., "Flow Oscillations of Spike-Tipped Bodies," *AIAA Journal*, Vol. 20, No. 1, 1981, pp. 25, 26.

[20]Ingram, C. L., McRae, D., and Benson, R., "Time-Accurate Simulation of a Self-Excited Oscillatory Supersonic External Flow with a Multi-Block Solution Adaptive Mesh Algorithm," AIAA Paper 93-3387-CP, 1993.

[21]Feszty, D., Badcock, K., and Richards, B., "Utilising CFD in the Investigation of High-Speed Spiked Body Flows," *Aeronautical Journal*, Vol. 106, No. 1058, 2002, pp. 161–174.

[22]Edney, B., "Effects of Shock Impingement on the Heat Transfer Around Blunt Bodies," *AIAA Journal*, Vol. 6, No. 1, 1968, pp. 15–21.

[23]Rockwell, D., and Naudascher, E., "Self-Sustained Oscillations of Impinging Free Shear Layers," *Annual Review of Fluid Mechanics*, Vol. 11, 1979, pp. 67–94.

[24]Badcock, K., Richards, B., and Woodgate, M., "Elements of Computational Fluid Dynamics on Block Structured Grids Using Implicit Solvers," *Progress in Aerospace Sciences*, Vol. 36, 2000, pp. 351–392.

[25]Gnoffo, P., "Point-Implicit Relaxation Strategies for Viscous Hypersonic Flows," *Computational Methods in Hypersonic Aerodynamics*, edited by T. K. S. Murthy, Kluwer Academic, Norwell, MA, 1993, pp. 115–151.

[26]"Equations, Tables, and Charts for Compressible Flow," NACA 1135, 1953.

[27]Ferri, A., and Nucci, L., "The Origin of Aerodynamic Instability of Supersonic Inlets at Subcritical Conditions," NACA RM L50 K30, Jan. 1951.

[28]Feszty, D., Badcock, K., Richards, B., and Woodgate, M., "Numerical Simulation of a Pulsating Flow Arising over an Axisymmetric Spiked Blunt Body at Mach 2.21 and Mach 6.00," *Shock Waves*, Vol. 10, No. 5, 2000, pp. 323–331.

[29]Feszty, D., "Numerical Simulation and Analysis of High-Speed Unsteady Spiked Body Flows," Ph.D. Dissertation, Dept. of Aerospace Engineering, Univ. of Glasgow, Glasgow, Scotland, U.K., 2001.

M. Sichel
Associate Editor